COMPUTING AND ALGORITHM INSIGHT
Volume 1, Issue 2, December 2023 | pp. 127-140
https://doi.org/10.63208/21018-100

OPEN ACCESS
Check for updates

GENERATIVE ADVERSARIAL NETWORKS FOR MITIGATING PARTIAL COHERENCE IN COHERENT DIFFRACTIVE IMAGING

Li Ming Xiao[1] ✉, Nguyen Thanh Tung[1], and Chen Yu Wei[2]

School of Computer Science and Engineering, Henan Polytechnic University, Jiaozuo, China[1]; College of Information Engineering, Yangzhou University, Yangzhou, China[2]

ABSTRACT

This paper presents a generative deep learning approach to mitigate image degradation caused by partial coherence in lensless Coherent Diffractive Imaging (CDI). While high-resolution CDI relies on ideal X-ray coherence, experimental constraints frequently introduce partial coherence, leading to blunted diffraction patterns. Unlike existing methods that require expensive computation or pre-calibration to model illumination coherence, our proposed Generative Adversarial Network (GAN) directly restores sharp structural features from degraded images without explicit coherence characterization. The effectiveness of this approach is validated through applications in both CDI and ptychography, indicating its potential utility for a wide spectrum of phase-retrieval-based imaging techniques.

Keywords: *Coherent Diffractive Imaging (CDI), Partial Coherence, Generative Adversarial Network (GAN), Phase Retrieval, Deep Learning.*

CORRESPONDING AUTHOR:
Li Ming Xiao
School of Computer Science and Engineering, Henan Polytechnic University, Jiaozuo, China
contact: *limingxiao@hpu.edu.cn*

ARTICLE HISTORY
Received : July 10, 2023
Final Revised : November 13, 2023
Accepted : December 5, 2023
Published : December 30, 2023

© 2023 The Author(s) | Published by **Integra Academic Press** | This article is an open access article and distributed under the terms and conditions of the Creative Commons Attribution (CC BY-SA) license.

1. | INTRODUCTION

Phase retrieval, which is the reconstruction of phase distributions from intensity measurements is fundamental to lensless imaging modalities, including coherent diffractive imaging (CDI) [1,2,3,4,5] and ptychography [6,7]. In standard CDI, a detector captures the diffraction pattern produced by illuminating a sample with coherent wavefields. The associated phase information is subsequently recovered using iterative algorithms [8,9], facilitating high-resolution two- or three-dimensional object reconstruction [10,11]. Ptychography, a scanning variant of CDI [12], records multiple far-field diffraction patterns from overlapping sample regions. These spatial overlaps serve as constraints within the iterative process to simultaneously reconstruct the object and the illumination function (the probe) [13].

A critical underlying assumption in both CDI and ptychography is the full coherence of the incident X-ray beam, which establishes a direct Fourier transform relationship between the object and the diffracted intensity. However, partial coherence leads to significant image degradation, manifested as reduced resolution, geometric inaccuracies, and structural defects. While third-generation synchrotron and free-electron laser sources provide highly coherent X-rays [14,15,16,17], various experimental uncertainties often result in sub-optimal coherence levels.

To mitigate the deleterious effects of partial coherence, traditional strategies have followed two primary paths: (1) integrating a priori knowledge of illumination coherence into the phase retrieval algorithm [18], or (2) dynamically recovering coherence properties during the iterative process [19,20]. Both approaches necessitate determining specific coherence parameters that vary with the X-ray source environment. The first method is limited by the requirement for preliminary experimental characterization [21], while the second relies on solving complex deconvolution problems, which typically succeed only when the initial illumination is sufficiently coherent [19].

In contrast to these established methods, we propose a framework based on Generative Adversarial Networks (GANs) to restore latent, fully coherent diffractive images directly from partially coherent inputs. This approach eliminates the need for additional experimental data or high baseline coherence. By treating the enhancement of partial coherence as a deblurring task within an image-to-image translation context, we leverage the capabilities of GANs, which have demonstrated significant success in image inpainting, denoising, and super-resolution [22,23,24,25]. Specifically, certain GAN architectures are highly effective at addressing ill-posed deblurring problems [26]. Our model employs a competitive training scheme where the generator produces coherence-enhanced images while the discriminator attempts to distinguish them from ground-truth coherent patterns. Through this process, the model learns to effectively restore the visibility and contrast of diffraction fringes.

Mathematically, it has been established that diffraction patterns under partial coherence can be described by the following expression [18,19,27]:

$$I_{pc}(q) = I_c(q) \otimes \hat{g}(q) \tag{1}$$

In this formulation, $I_{pc}(q)$ denotes the partially coherent diffraction pattern, while $I_c(q)$ represents the corresponding fully coherent diffraction image. The symbol $\otimes$ denotes the convolution operator, and $\hat{g}(q)$ signifies the Fourier transform of the mutual coherence function (MCF), which characterizes the coherence properties of the system. This mathematical framework establishes a direct analogy to classical image degradation models,

where a blurred observation is represented as the convolution of a latent sharp image with a specific blur kernel.

$$I_B = I_S \otimes K_B \tag{2}$$

In this context, $I_B and I_S$ denote the blurred and sharp images, respectively, while K_B represents the blur kernel. Under this framework, both partially coherent diffractive patterns and blurred images are interpreted as degraded versions of their respective ground truths—fully coherent diffractive images and sharp images—resulting from convolution with a specific kernel.

For the purposes of training and evaluation in this study, the dataset was synthesized. Sharp images, serving as the fully coherent diffractive patterns, were generated by applying a Fourier transform to the source image dataset. To simulate partially coherent diffractive images, these fully coherent patterns were subsequently convolved with a Gaussian blur kernel. Following the training phase, the proposed model is capable of generating coherence-enhanced diffractive images from these partially coherent inputs.

2. | PROPOSED APPROACH

2.1. Conditional GAN

The Generative Adversarial Network (GAN) was originally introduced by Goodfellow et al. [28] as a framework for training generative models through an adversarial procedure. As previously noted, the architecture comprises two competing neural networks: the generator and the discriminator. The generator is tasked with producing a synthetic ("fake") image from a given input noise vector z. Conversely, the discriminator functions as a classifier that estimates the probability that a sample originates from the actual training dataset rather than the generator's output. These two components undergo simultaneous training, evolving until the discriminator can no longer differentiate between real data and generated samples. This adversarial interaction is mathematically formalized as a two-player minimax game, defined by the following objective function:

$$\min_G \max_D V(D,G) = E_{x\sim p_{\mathrm{dt}}(x)}[\log D(x)] + E_{z\sim p_z(z)}\left[\log\left(1 - D\big(G(z)\big)\right)\right] \tag{3}$$

In this formulation, P_{data} represents the distribution of the training data x, and P_z denotes the distribution of the input noise vector z. While the original GAN lacks a mechanism to constrain the generated output, the conditional GAN (cGAN) [29] introduces greater flexibility, enabling effective general image-to-image translation [30]. By incorporating a conditional variable c into both the generator and discriminator, the cGAN architecture directs the synthesis process toward user-specified content.

This supervised approach is particularly advantageous for synthesizing diffraction patterns, which are characterized by a central peak intensity that decays toward the peripheral regions. By conditioning the generative process on these specific domain characteristics, the model can more accurately produce diffraction patterns consistent with experimental observations. Consequently, the modified objective function for the conditional GAN is defined as follows:

$$\min_G \max_D V(D,G) = E_{x\sim p_{\mathrm{dt}}(x)}[\log D(x,c)] + E_{z\sim p_z(z)}\big[\log\big(1 - D(G(z,c),c)\big)\big] \tag{4}$$

To optimize the training of the conditional GAN for the deblurring of diffractive images, we adopted the approach established by Kupyn et al. [26], which incorporates Wasserstein loss with gradient penalty [31,32] alongside perceptual loss [33]. The integration of Wasserstein

loss ensures a more stable and effective adversarial training process by mitigating issues such as mode collapse and vanishing gradients. Complementarily, the inclusion of perceptual loss—often derived from high-level features of pretrained networks—is instrumental in achieving high-fidelity results, particularly in tasks involving style transfer and structural restoration.

2.2. Coherence-Enhanced GAN

In our GAN framework, the generator receives partially coherent diffractive patterns as input to produce coherence-enhanced counterparts. The architectural details of the generator's convolutional neural network are illustrated in Figure 1a. The initial stage utilizes three convolutional layers for feature extraction from the input images, while the final stage employs two deconvolutional layers followed by a convolutional layer to reconstruct the restored image.

The central architecture consists of nine residual blocks (ResBlocks) [34], each comprising two convolutional layers. Within these blocks, the first convolution is followed by batch normalization and a ReLU activation function, while the second convolution is followed solely by batch normalization. The resulting output is subsequently summed with the original block input, a design choice that enhances the efficiency and speed of feature extraction. Furthermore, a global skip connection is implemented [35,36], directly adding the network input to the output. This allows the generator to focus on learning the residual mapping between partially and fully coherent diffractive images. Given the high degree of feature similarity between the input and target images, learning only the residuals is computationally more efficient. The generator's design is modeled after DeblurGAN [26].

Concurrently, the discriminator is tasked with distinguishing the coherence-enhanced images from the ground-truth fully coherent patterns. Throughout the training process, the discriminator facilitates the generator's refinement by providing adversarial loss feedback. As shown in Figure 1b, the discriminator employs a PatchGAN architecture [37,38], which has been demonstrated to be more effective for deblurring tasks than conventional discriminator models [39].

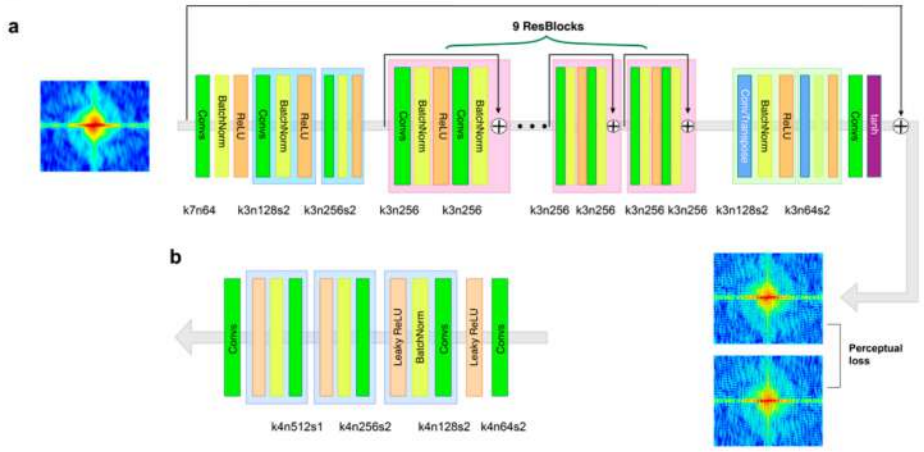


Figure 1. Detailed internal structure of the GAN components: (a) generator network and (b) PatchGAN-based discriminator, with corresponding kernel size (k), filter count (n), and stride (s) indicated for the respective layers.

2.3. Loss Functions

The loss function is composed of two primary components: (a) the adversarial loss (L_{GAN}), which directs the generator network toward the target transformation, and (b) the content loss (L_X), which ensures the preservation of structural and semantic integrity within the images.

$$L = L_{GAN} + \lambda L_X \tag{5}$$

In this formulation, λ serves as a balancing hyperparameter, assigned a value of 100. The adversarial loss is strategically designed to compel the network to synthesize fully coherent diffractive patterns capable of deceiving the discriminator, thereby ensuring the generated outputs remain statistically consistent with the target distribution.

$$L_{GAN} = \sum_{n=1}^{N} -D_{\theta_D}\left(G_{\theta_G}(I_B)\right) \tag{6}$$

Perceptual loss is significantly more effective at preserving intricate image textures than pixel-wise error metrics, such as L_1 (mean absolute error) or L_2 (mean squared error). While pixel-based losses tend to average out high-frequency details resulting in overly smoothed or "blurry" reconstructions perceptual loss encourages the model to maintain the structural and feature-based integrity of the diffraction fringes, which is critical for high-fidelity phase retrieval.

$$L_X = \frac{1}{W_{i,j}H_{i,j}} \sum_{x=1}^{W_{i,j}} \sum_{y=1}^{H_{i,j}} \left[\phi_{i,j}(I_S)_{x,y} - \phi_{i,j}\left(G_{\theta_G}(I_B)\right)_{x,y}\right]^2 \tag{7}$$

Equation (7) represents the L_2 norm (Euclidean distance) between the feature maps of the ground truth and the deblurred image extracted from a specific layer of the VGG-19 network [40]. Here, $\phi_{i,j}$ signifies the feature map obtained at the j-th convolutional layer prior to the i-th max-pooling operation within the VGG-19 architecture, which was pre-trained on the ImageNet dataset [41]. In this context, I_S and I_B denote the ground truth and the predicted frame, respectively, while $W_{i,j}$ and $H_{i,j}$ correspond to the width and height dimensions of the respective feature maps. For this study, the $VGG_{3,3}$ convolutional layer was selected for feature extraction [39]. Furthermore, since the network architecture requires color image inputs, the grayscale diffractive images were replicated across three channels to populate the RGB input space.

3. | IMAGE SYNTHESIS FOR COMPUTATIONAL EXPERIMENTS

3.1. Synthesis of Partially Coherent Diffractive Images

In this study, the diffraction phenomenon is modeled within the kinetic regime, analytically characterized by the classical formulation of kinetic X-ray scattering from crystalline materials [42]. Consequently, fully coherent diffractive patterns are simulated via the Fourier transformation of an image dataset, while partially coherent patterns are synthesized through convolution with a Gaussian blur kernel [43]. To facilitate effective model training, these diffractive images are transformed to a logarithmic scale and subsequently reverted to a linear scale for the phase retrieval process.

The experimental data is derived from a publicly available dataset of English alphabet characters [44]. The training set comprises 13,920 pairs of grayscale images, while the evaluation set consists of 310 samples uniformly distributed across the 26 letters of the alphabet. The original 28 × 28 pixel images were resampled to 64 × 64 pixels using bicubic interpolation and further expanded to a 256 × 256 pixel format through zero-padding. The resulting ratio between the total image area and the object region establishes an oversampling ratio of 4. This configuration ensures that the diffraction patterns can be successfully inverted to reconstruct the object via phase retrieval, as the oversampling ratio exceeds the minimum requirement of 2 stipulated for CDI image reconstruction [1].

The two-dimensional representation of the relationship described in Equation (1) is formulated as follows:

$$I_{pc}(q_x, q_y) = I_c(q_x, q_y) \otimes \hat{g}(q_x, q_y) \tag{8}$$

The mutual coherence function (MCF) is defined within the reciprocal space according to the following expression, as it is accurately approximated by a Gaussian distribution [42]:

$$\hat{g}(q_x, q_y) = A \cdot \exp\left(-\frac{(q_x - q_o)^2}{2\widehat{\sigma_x^2}} - \frac{(q_y - q_o)^2}{2\widehat{\sigma_y^2}}\right) \tag{9}$$

In this formulation, the coefficient \$A\$ represents the amplitude, while $\widehat{\sigma_x}$ and $\widehat{\sigma_y}$ denote the standard deviations along the q_x and q_y axes, respectively. These standard deviations are the primary parameters governing the degree of blurriness in the synthesized images.

Figure 2a–c illustrates the components of this process: (a) a fully coherent diffractive image, (b) the corresponding blur kernel $\hat{g}(q_x, q_y)$ with a standard deviation of 2 along both the q_x and q_y directions, and (c) the resulting degraded image. To further analyze the impact of the kernel, Figure 2d presents line-outs extracted through the center of the diffraction patterns along the q_y direction, highlighting the loss of fringe contrast. The specific blur kernel depicted in Figure 2b was utilized consistently across all input images during the model training phase.

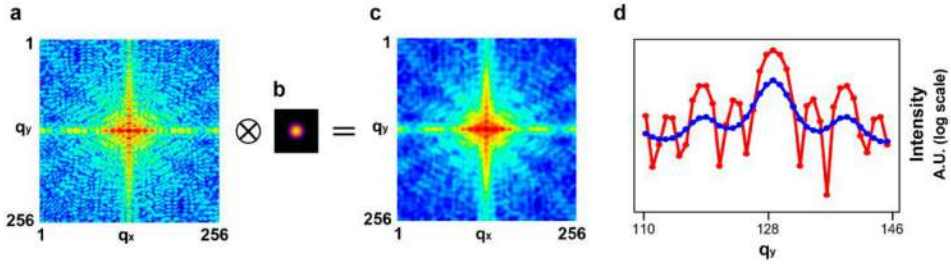


Figure 2. Generation of degraded diffraction data. (a) Ground-truth fully coherent diffraction pattern. (b) Gaussian blur kernel ($\sigma = 2$) used as the degradation operator. (c) Synthesized partially coherent image after convolution. (d) Intensity profiles (line-outs) across the center of the images in (a) and (c), illustrating the reduction in fringe visibility due to partial coherence.

3.2. Degree of Coherence

The spatial coherence length, characterized by the standard deviation σ of the Mutual Coherence Function (MCF) in real space, can be estimated using the relationship $\sigma = N/(2\pi\hat{\sigma})$. Given an image dimension of $N = 256$ pixels and a blur kernel standard deviation of $\hat{\sigma} = 2$, the resulting real-space σ is approximately 20.

Conventional restoration techniques that rely on coherence property corrections are typically constrained by the spatial extent of the coherence. Specifically, it is generally required that the normalized MCF remains non-zero over a width at least twice the dimensions of the object [19]. In this study, the normalized MCF with a standard deviation of 20 yields a value of only 0.007 at ± 64 pixels, which corresponds to the boundary of twice the object's size. Because the coherence barely satisfies this fundamental criterion, the level of degradation represented by a standard deviation of $\hat{\sigma} = 2$ in reciprocal space poses a significant challenge for traditional iterative refinement methods that depend on coherence property adjustments [19].

4. | MODEL VALIDATION AND DISCUSSION

4.1. Model Details and Parameters

The proposed model was implemented using the PyTorch framework, with all numerical experiments conducted on an NVIDIA Tesla K80 GPU. A consistent learning rate of 10^{-4} was maintained for both the generator and the discriminator. The performance of the GAN was evaluated initially in the reciprocal space—the original domain of the data—and subsequently in real space via image reconstruction through Coherent Diffractive Imaging (CDI) and ptychography.

To quantify the fidelity of the coherence-enhanced diffraction patterns relative to the ground-truth fully coherent images, the Structural Similarity Index Measure (SSIM) [45] and the Peak Signal-to-Noise Ratio (PSNR) were utilized. The SSIM index is a normalized metric ranging from 0 to 1, where a value of 1 indicates identical structural characteristics and 0 signifies a total lack of similarity. Training was concluded at epoch 80, at which point both the SSIM and PSNR metrics reached a stable plateau, as illustrated in Figure 3a.

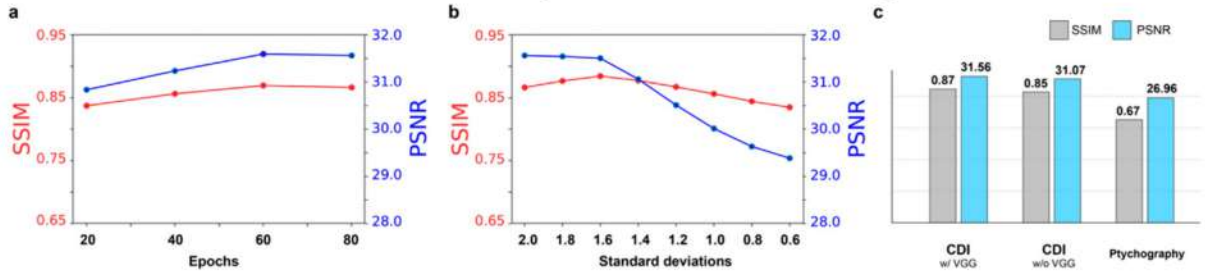


Figure 3. Evaluation of model performance through SSIM and PSNR. (a) Training stability achieved by epoch 80. (b) Sensitivity analysis of the model (trained at $\sigma = 2$) when subjected to fluctuating levels of blurriness. (c) Performance comparison between configurations with and without perceptual loss. A performance decline is noted during ptychographic application. Average metrics are derived from 310 CDI test images and 6 ptychography-specific samples utilized in this study.

4.2. Comparison of Performance

The model, trained on diffractive patterns degraded by a Gaussian blur kernel with a standard deviation of 2, was evaluated across a spectrum of coherence levels. As illustrated in Figure 3b, the network exhibits significant robustness; despite deviations in the degree of coherence from the training parameters, both PSNR and SSIM metrics remain consistently high.

Furthermore, the GAN model originally developed for CDI was extended to ptychographic imaging. This application introduced two primary textural discrepancies compared to the training set. First, the oversampling ratio in ptychography is inherently lower than in CDI, as the X-ray illumination typically does not isolate the entire object. Second, the ptychographic diffraction patterns in this study were generated from multiple characters, whereas the training dataset was restricted to single letters. These stylistic variations in the input data resulted in a marginal reduction in SSIM and PSNR values, as depicted in Figure 3c. Finally, the results indicate that the integration of perceptual loss, which leverages an external feature-extraction network [41] to recover intricate textural details substantially enhances the model's restorative capacity.

4.3. Performance of Coherent Diffractive Imaging

Phase retrieval was performed using three distinct categories of diffraction data: fully coherent, partially coherent, and coherence-enhanced images, as depicted in Figure 4a. The results demonstrate that reconstruction performance is substantially improved when utilizing the coherence-enhanced diffractive patterns. As shown in Figure 4b, the object reconstructed from the coherence-enhanced data is nearly identical to the ground truth obtained from fully coherent patterns, whereas reconstruction attempts using partially coherent data failed to yield recognizable results.

These findings indicate that the GAN model accurately restores the original diffraction fringes, enabling successful phase retrieval in scenarios where it would otherwise be unfeasible. For the reconstruction process, we employed alternating projection-based algorithms, which are foundational to phase retrieval. Specifically, the classical Gerchberg–Saxton error reduction (ER) [46] and Fienup's hybrid input–output (HIO) [47] methods were utilized to enforce amplitude constraints in both reciprocal and real space.

$$\rho^{(n+1)} = P_s P_m \rho^{(n)} \tag{10}$$

In this formulation, $\rho^{(n)}$ represents the object density at the n-th iteration, while P_s and P_m denote the projection operators in real and reciprocal space, respectively. The support projector, P_s, enforces spatial constraints by setting the object density to zero for all coordinates residing outside a predefined region known as the support. Conversely, the modulus projector, P_m, operates on the Fourier transform of the density. In this stage, the calculated Fourier magnitudes are substituted with the square root of the measured (or enhanced) diffraction intensities. The phase retrieval procedure in this study consisted of 500 iterations, incorporating the "shrink-wrap" algorithm [48] to periodically update and refine the object support based on the evolving density.

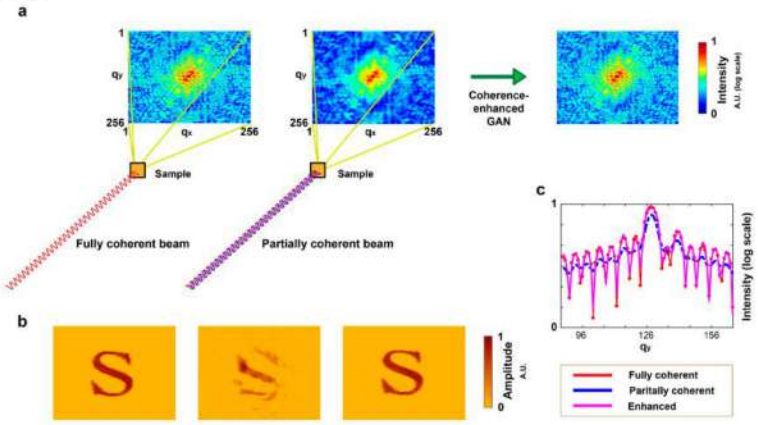


Figure 4. Performance of the GAN model in transmission-mode CDI. (a) Comparison between ground-truth coherent, degraded partially coherent, and GAN-restored diffractive images. (b) Reconstructed object images; the failure of the partially coherent data (middle) contrasts with the high-fidelity reconstruction from the coherence-enhanced data (right), which mirrors the fully coherent result (left). Reconstructions are displayed as 128 × 128 pixel crops. (c) Horizontal line-outs through the diffraction center, demonstrating the quantitative accuracy of the restored fringes.

4.4. Performance of Ptychography

Ptychographic reconstruction is achieved through the simultaneous inversion of a collection of overlapping diffraction patterns. In the data acquisition phase, a localized illumination probe translates across the specimen, recording far-field diffraction intensities at

each scan position. For this study, the extended Ptychographic Iterative Engine (ePIE) algorithm [49] was implemented. The ePIE procedure begins with an initial estimate for both the object function, $O_0(r)$, and the illumination probe, $P_0(r)$. The algorithm processes the diffraction patterns sequentially; for each position, an estimate of the exit-surface wave is generated by calculating the product of the current object estimate and the appropriately shifted probe estimate.

$$\psi i(r) = Oi(r)Pi\big(r - rs(i)\big) \tag{11}$$

In this formulation, the i-th exit-surface wave is defined as $\psi_i(r)$, where r denotes the real-space coordinate vectors. The illumination probe and the object's transmission function are represented by $P(r)$ and $O(r)$, respectively. The vector $r_{s(i)}$ signifies the relative spatial displacement between the probe and the object at the i-th scan position. Consistent with the modulus projector P_m described in Equation (10), the magnitude of the Fourier-transformed exit wave is substituted with the square root of the measured (or coherence-enhanced) intensity recorded at the $s(i)$-th position. This constraint ensures that the reconstructed wavefront remains consistent with the experimental diffraction data while the phase information is iteratively recovered.

$$\Psi_i(u) = \sqrt{I_{s(i)}(u)}\,\frac{\mathcal{F}[\psi_i(r)]}{|\mathcal{F}[\psi_i(r)]|} \tag{12}$$

An updated estimate of the exit-surface wave in real space is subsequently obtained by performing an inverse Fourier transform on the corrected reciprocal-space wavefront:

$$\psi_i'(r) = \mathcal{F}^{-1}[\Psi_i(u)] \tag{13}$$

The updated estimates for the object transmission function and the illumination probe are subsequently refined using the following two update functions:

$$O_{i+1}(r) = O_i(r) + \alpha\frac{P_i^*(r-r_{s(i)})}{|P_i(r-r_{s(i)})|^2_{max}}[\psi_i'(r) - \psi_i(r)] \tag{14}$$

$$P_{i+1}(r) = P_i(r) + \beta\frac{O_i^*(r+r_{s(i)})}{|O_i(r+r_{s(i)})|^2_{max}}[\psi_i'(r) - \psi_i(r)] \tag{15}$$

In this study, the convergence step parameters α and β were both set to 1. The iterative refinement of the object and probe functions depends heavily on the use of fully coherent illumination and a sufficient overlap between adjacent scan positions. Figure 5a illustrates the ptychographic experimental configuration, where six diffractive patterns were recorded as the object shifted, maintaining an overlap ratio of 73%.

The illumination probe was modeled as an ellipse with major and minor axes of 140 and 100 pixels, respectively. This geometry results in oversampling ratios of 2.2 in the longitudinal direction and 1 in the transverse direction—values that differ significantly from the uniform oversampling ratio of 4 employed in the CDI experiments.

Figure 5b–d present the comparative diffraction data: (b) the ground-truth fully coherent patterns, (c) the partially coherent patterns synthesized via convolution with the Gaussian kernel from Figure 2b, and (d) the corresponding coherence-enhanced patterns generated by the GAN. A detailed comparison of the first image from each set is provided in the enlarged views of Figure 5e.

Finally, Figure 5f displays the real-space reconstructions. While the reconstruction using partially coherent data fails to resolve the object, the GAN-enhanced data yields a reasonably accurate and high-quality solution. This demonstrates that despite being trained specifically on

CDI data, the GAN model generalizes effectively to the distinct image textures and sampling constraints inherent in ptychographic imaging.

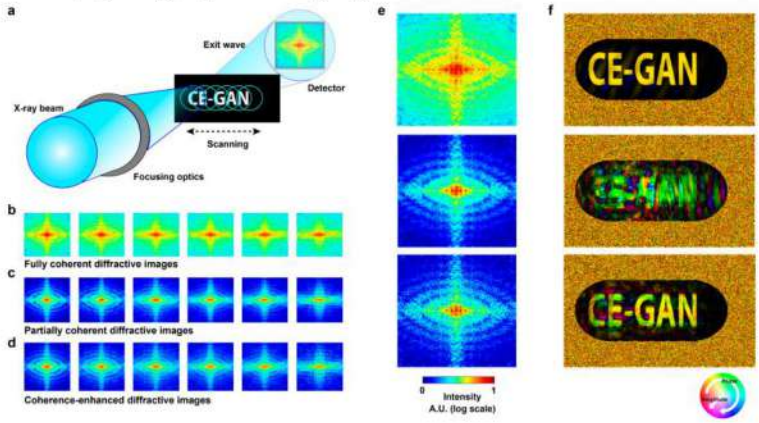


Figure 5. Quantitative assessment of the coherence-enhancement GAN in ptychographic imaging. (a) Schematic representation of the ptychographic experimental configuration, where a two-dimensional specimen is scanned using a focused beam under varying coherence states while far-field diffraction intensities are recorded. A 73% spatial overlap is maintained between adjacent illumination positions. (b–d) Sets of six diffraction patterns corresponding to fully coherent, partially coherent, and coherence-enhanced illumination, respectively. (e) High-magnification views of the initial diffraction patterns from sets (b), (c), and (d), arranged vertically for comparative analysis of fringe restoration. (f) Real-space object reconstructions derived from the three data categories: fully coherent, partially coherent (exhibiting reconstruction failure), and GAN-enhanced diffraction patterns (demonstrating successful restoration), arranged from top to bottom.

4.5. Discussion

In this study, we have demonstrated that a coherence-enhanced GAN significantly improves the quality of partially coherent diffractive data. This improvement is quantified by high SSIM and PSNR values in the reciprocal space and validated by high-fidelity object reconstructions in real space via both CDI and ptychography.

The level of partial coherence examined here presents a significant challenge for conventional iterative techniques. However, our findings reveal that a model trained on a specific degree of decoherence maintains robust performance when applied to images with even higher degrees of partial coherence. This suggests that training the network on a "worst-case" scenario of degradation enables it to generalize across a wide spectrum of image qualities. Furthermore, the GAN model appears to be insensitive to variations in oversampling ratios. Consequently, this coherence-enhancement approach provides a reliable and precise input for phase retrieval algorithms, effectively bridging the gap between non-ideal experimental conditions and successful image reconstruction in both CDI and ptychography.

5. | CONCLUSION

In summary, this work introduces a Generative Adversarial Network (GAN) specifically designed to enhance partially coherent diffractive patterns. While lensless coherent diffractive imaging (CDI) fundamentally necessitates fully coherent data for successful phase retrieval, experimental uncertainties often degrade the coherence of X-ray beams. Such partial coherence traditionally limits the precision of image reconstructions, necessitating rigorous mitigation strategies.

Departing from conventional iterative correction methods, our GAN-based approach is trained to directly restore fringe visibility and contrast within the diffraction intensities. Given its robust performance across varying degrees of decoherence, this model offers a versatile solution applicable to a broad spectrum of lensless imaging modalities.

REFERENCES

1. Miao, J.; Charalambous, P.; Kirz, J.; Sayre, D. Extending the methodology of X-ray crystallography to allow imaging of micrometre-sized non-crystalline specimens. *Nature* 1999, 400, 342–344.
2. Robinson, I.; Harder, R. Coherent X-ray Diffraction Imaging of Strain at the Nanoscale. *Nat. Mater.* 2009, 8, 291–298.
3. Williams, G.J.; Pfeifer, M.A.; Vartanyants, I.A.; Robinson, I.K. Three-Dimensional Imaging of Microstructure in Au Nanocrystals. *Phys. Rev. Lett.* 2003, 90, 175501.
4. Kim, J.W.; Manna, S.; Dietze, S.; Ulvestad, A.; Harder, R.; Fohtung, E.; Fullerton, E.; Shpyrko, O. Curvature-induced and thermal strain in polyhedral gold nanocrystals. *Appl. Phys. Lett.* 2014, 105, 173108.
5. Kim, J.W.; Ulvestad, A.; Manna, S.; Harder, R.; Fullerton, E.E.; Shpyrko, O.G. 3D Bragg coherent diffractive imaging of five-fold multiply twinned gold nanoparticle. *Nanoscale* 2017, 9, 13153–13158.
6. Seaberg, M.D.; Zhang, B.; Gardner, D.F.; Shanblatt, E.R.; Murnane, M.M.; Kapteyn, H.R.; Adams, D.E. Tabletop nanometer extreme ultraviolet imaging in an extended reflection mode using coherent Fresnel ptychography. *Optica* 2014, 1, 39–44.
7. Rodenburg, J.M. Ptychography and related diffractive imaging methods. *Adv. Imaging Electron Phys.* 2008, 150, 87.
8. Fienup, J.R.; Marron, J.C.; Schulz, T.J.; Seldin, J.H. Hubble space telescope characterized by using phase-retrieval algorithms. *Appl. Opt.* 1993, 32, 1747.
9. Miao, J.; Kirz, J.; Sayre, D. The oversampling phasing method. *Acta Crystallogr. D* 2000, 56, 1312.
10. Chapman, H.N.; Nugent, K.A. Coherent lensless X-ray imaging. *Nat. Photon.* 2010, 4, 833–839.
11. Pfeifer, M.A.; Williams, G.J.; Vartanyants, I.A.; Harder, R.; Robinson, I.K. Three-dimensional mapping of a deformation field inside a nanocrystal. *Nature* 2006, 442, 63–66.
12. Rodenburg, J.M.; Faulkner, H.M.L. A phase retrieval algorithm for shifting illumination. *Appl. Phys. Lett.* 2004, 85, 4795–4797.
13. Thibault, P.; Dierolf, M.; Bunk, O.; Menzel, A.; Pfeiffer, F. Probe retrieval in ptychographic coherent diffractive imaging. *Ultramicroscopy* 2009, 109, 338–343.
14. Xiong, G.; Moutanabbir, O.; Reiche, M.; Harder, R.; Robinson, I. Coherent X-ray diffraction imaging and characterization of strain in silicon-on-insulator nanostructures. *Adv Mater.* 2014, 26, 7747–7763.
15. Williams, G.J.; Quiney, H.M.; Peele, A.G.; Nugent, K.A. Coherent diffractive imaging and partial coherence. *Phys. Rev. B* 2007, 75, 104102.

16. Vartanyants, I.A.; Singer, A. Coherence properties of hard X-ray synchrotron sources and free-electron lasers. *New J. Phys.* 2010, 12, 035004.
17. Graves, W.S.; Bessuille, J.; Brown, P.; Carbajo, S.; Dolgashev, V.; Hong, K.-H.; Ihloff, E.; Khaykovich, B.; Lin, H.; Murari, K.; et al. Compact X-ray source based on burst-mode inverse Compton scattering at 100 kHz. *Phys. Rev. ST Accel. Beams* 2014, 17, 120701.
18. Whitehead, L.W.; Williams, G.J.; Quiney, H.M.; Vine, D.J.; Dilanian, R.A.; Flewett, S.; Nugent, K.A.; Peele, A.G.; Balaur, E.; McNulty, I. Diffractive imaging using partially coherent X-rays. *Phys. Rev. Lett.* 2009, 103, 243902.
19. Clark, J.N.; Huang, X.; Harder, R.; Robinson, I.K. High-resolution three-dimensional partially coherent diffraction imaging. *Nat. Commun.* 2012, 3, 993.
20. Clark, J.N.; Peele, A.G. Simultaneous sample and spatial coherence characterization using diffractive imaging. *Appl. Phys. Lett.* 2011, 99, 154103.
21. Parks, D.H.; Shi, X.; Kevan, S.D. Partially coherent X-ray diffractive imaging of complex objects. *Phys. Rev. A* 2014, 89, 063824.
22. Jiang, Y.; Xu, J.; Yang, B.; Xu, J.; Zhu, J. Image inpainting based on generative adversarial networks. *IEEE Access* 2020, 8, 22884–22892.
23. Wolterink, J.M.; Leiner, T.; Viergever, M.A.; Isgum, I. Generative adversarial networks for noise reduction in low-dose CT. *IEEE Trans Med Imaging* 2017, 36, 2536–2545.
24. Karras, T.; Laine, S.; Aila, T. A style-based generator architecture for generative adversarial networks. In *Proceedings of the IEEE CVPR*, Long Beach, CA, USA, 15–20 June 2019; pp. 4401–4410.
25. Ledig, C.; Theis, L.; Huszar, F.; Caballero, J.; Cunningham, A.; Acosta, A.; Aitken, A.; Tejani, A.; Totz, J.; Wang, Z.; et al. Photo-realistic single image super-resolution using a generative adversarial network. In *Proceedings of the IEEE CVPR*, Honolulu, HI, USA, 21–26 July 2017; pp. 4681–4690.
26. Kupyn, O.; Budzan, V.; Mykhailych, M.; Mishkin, D.; Matas, J. DeblurGAN: Blind motion deblurring using conditional adversarial networks. In *Proceedings of the IEEE CVPR*, Salt Lake City, UT, USA, 18–22 June 2018; pp. 8183–8192.
27. Tran, C.Q.; Peele, A.G.; Roberts, A.; Nugent, K.A.; Paterson, D.; McNulty, I. Synchrotron beam coherence: A spatially resolved measurement. *Opt. Lett.* 2005, 30, 204.
28. Goodfellow, I.; Pouget-Abadie, J.; Mirza, M.; Xu, B.; Warde-Farley, D.; Ozair, S.; Courville, A.; Bengio, Y. Generative adversarial nets. In *Advances Neural Information Processing Systems*; MIT Press: Cambridge, MA, USA, 2014; p. 27.
29. Mirza, M.; Osindero, S. Conditional generative adversarial nets. *arXiv* 2014, arXiv:1411.1784.
30. Ronneberger, O.; Fischer, P.; Brox, T. U-Net: Convolutional networks for biomedical image segmentation. In *Proceedings of the International Conference on Medical Image Computing and Computer-Assisted Intervention*, Munich, Germany, 5–9 October 2015; Springer: Cham, Switzerland, 2015; pp. 234–241.
31. Arjovsky, M.; Chintala, S.; Bottou, L. Wasserstein GAN. *arXiv* 2017, arXiv:1701.07875.
32. Gulrajani, I.; Ahmed, F.; Arjovsky, M.; Dumoulin, V.; Courville, A. Improved Training of Wasserstein GANs. In *Advances in Neural Information Processing Systems*; MIT Press: Cambridge, MA, USA, 2017; p. 30.
33. Johnson, J.; Alahi, A.; Fei-Fei, L. Perceptual losses for real-time style transfer and super-resolution. In *Proceedings of the European Conference on Computer Vision*, Munich, Germany, 8–14 September 2016.

34. He, K.; Zhang, X.; Ren, S.; Sun, J. Deep residual learning for image recognition. *arXiv* 2015, arXiv:1512.03385.
35. Kim, J.; Lee, J.K.; Lee, K.M. Accurate image super-resolution using very deep convolutional networks. In *Proceedings of the IEEE CVPR*, Las Vegas, NV, USA, 27–30 June 2016; pp. 1646–1654.
36. Ramakrishnan, S.; Pachori, S.; Gangopadhyay, S.; Raman, S. Deep generative filter for motion deblurring. In *Proceedings of the IEEE CVPR*, Honolulu, HI, USA, 21–26 July 2017; pp. 2993–3000.
37. Isola, P.; Zhu, J.-Y.; Zhou, T.; Efros, A.A. Image-to-image translation with conditional adversarial network. *arXiv* 2016, arXiv:1611.07004.
38. Li, C.; Wand, M. Precomputed real-time texture synthesis with Markovian generative adversarial networks. In *Proceedings of the European Conference on Computer Vision*, Munich, Germany, 8–14 September 2016; Springer: Cham, Switzerland, 2016; pp. 702–716.
39. Feng, H.; Guo, J.; Xu, H.; Ge, S.S. SharpGAN: Dynamic scene deblurring method for smart ship based on receptive field block and generative adversarial networks. *Sensors* 2021, 21, 3641.
40. Simonyan, K.; Zisserman, A. Very deep convolutional networks for large-scale image recognition. *arXiv* 2014, arXiv:1409.1556.
41. Deng, J.; Dong, W.; Socher, R.; Li, L.-J.; Li, K.; Fei-Fei, L. ImageNet: A Large-Scale Hierarchical Image Database. In *Proceedings of the CVPR09*, Miami, FL, USA, 20–25 June 2009.
42. Vartanyants, I.A.; Robinson, I.K. Partial coherence effects on the imaging of small crystals using coherent X-ray diffraction. *J. Phys. Condens. Matter* 2001, 13, 10593–10611.
43. Maddali, S.; Allain, M.; Cha, W.; Harder, R.; Park, J.-S.; Kenesei, R.; Almer, J.; Nashed, Y.; Hruszkewycz, S.O. Phase retrieval for Bragg coherent diffraction imaging at high X-ray energies. *Phys. Rev. A* 2019, 99, 053838.
44. Lin, T.; Asokan, R. Alphabet Characters Fonts Dataset. Available online: https://www.kaggle.com/thomasqazwsxedc/alphabet-characters-fonts-dataset (accessed on 10 November 2021).
45. Wang, Z.; Bovik, A.C.; Sheikh, H.R.; Simoncelli, E.P. Image quality assessment: From error visibility to structural similarity. *IEEE Trans. Image Process.* 2004, 13, 600–612.
46. Fienup, J.R. Reconstruction of an object from the modulus of its Fourier transform. *Opt. Lett.* 1978, 3, 27–29.
47. Fienup, J.R. Reconstruction of a complex-valued object from the modulus of its Fourier transform using a support constraint. *J. Opt. Soc. Am. A* 1987, 4, 118–123.
48. Marchesini, S.; He, H.; Chapman, H.N.; Hau-Riege, A.P.; Noy, A.; Howells, M.R.; Weierstall, U.; Spence, J.C.H. X-ray image reconstruction from a diffraction pattern alone. *Phys. Rev. B* 2003, 68, 140101.
49. Maiden, A.M.; Rodenburg, J.M. An improved ptychographical phase retrieval algorithm for diffractive imaging. *Ultramicroscopy* 2009, 109, 1256–1262.